Thermal and vibrational properties of thermoelectric ZnSb: Exploring the origin of low thermal conductivity

A. Fischer,[1] E.-W. Scheidt,[1] W. Scherer,[1] D. E. Benson,[2] Y. Wu,[3,*] D. Eklöf,[4] and U. Häussermann[4]
[1]*Department of Physics, Augsburg University, D-86159 Augsburg, Germany*
[2]*Department of Physics, Arizona State University, Tempe, Arizona 85287-1504, USA*
[3]*Department of Chemistry and Biochemistry, Arizona State University, Tempe, Arizona 85287-1604, USA*
[4]*Department of Materials and Environmental Chemistry, Stockholm University, S-10691 Stockholm, Sweden*
(Received 20 February 2015; published 22 June 2015)

The intermetallic compound ZnSb is an interesting thermoelectric material largely due to its low lattice thermal conductivity. The origin of the low thermal conductivity has so far been speculative. Using multitemperature single crystal x-ray diffraction (9–400 K) and powder x-ray diffraction (300–725 K) measurements, we characterized the volume expansion and the evolution of structural properties with temperature and identified an increasingly anharmonic behavior of the Zn atoms. From a combination of Raman spectroscopy and first principles calculations of phonons, we consolidate the presence of low-energy optic modes with wave numbers below 60 cm^{-1}. Heat capacity measurements between 2 and 400 K can be well described by a Debye-Einstein model containing one Debye and two Einstein contributions with temperatures $\Theta_D = 195$ K, $\Theta_{E1} = 78$ K, and $\Theta_{E2} = 277$ K as well as a significant contribution due to anharmonicity above 150 K. The presence of a multitude of weakly dispersed low-energy optical modes (which couple with the acoustic, heat carrying phonons) combined with anharmonic thermal behavior provides an effective mechanism for low lattice thermal conductivity. The peculiar vibrational properties of ZnSb are attributed to its chemical bonding properties, which are characterized by multicenter bonded structural entities. We argue that the proposed mechanism to explain the low lattice thermal conductivity of ZnSb might also control the thermoelectric properties of other electron poor semiconductors, such as Zn_4Sb_3, CdSb, Cd_4Sb_3, $Cd_{13-x}In_yZn_{10}$, and $Zn_5Sb_4In_{2-\delta}$.

DOI: 10.1103/PhysRevB.91.224309 PACS number(s): 65.40.Ba, 65.40.De, 63.20.D−, 61.05.cp

I. INTRODUCTION

The binary Zn-Sb system affords two semiconductor phases, ZnSb and β-Zn_4Sb_3, which have been known as thermoelectric materials since the 1960s [1,2]. Especially β-Zn_4Sb_3 shows an excellent thermoelectric performance in the temperature range of 450–650 K and has been intensively studied during the past 15 years [3,4]. This material is distinguished by an extraordinarily low lattice thermal conductivity in the range of 0.5–0.6 W/mK at room temperature (RT), which is characteristic for vitreous materials [5]. Accordingly, this feature is truly remarkable for a crystalline binary compound. Recently it has been shown that ZnSb also has an inherently low thermal conductivity [6] and that doping with Ag/Cu (leading to Cu_3Sb and Ag_3Sb nanoparticle inclusions) can produce materials with thermoelectric figure of merits almost in par with β-Zn_4Sb_3 [7,8].

The origin of the low lattice thermal conductivity of β-Zn_4Sb_3 and ZnSb is puzzling. Constituting elements are not particularly heavy. In 2004 a careful structural analysis of β-Zn_4Sb_3 revealed intricately disordered Zn atoms. Naturally, this structural disorder was then associated with low thermal conductivity [9]. However, the discovery of $Cd_{13-x}In_yZn_{10}$ ($x \approx 2.7$, $y \approx 1.5$), which crystallizes in a disorder-free variant of the β-Zn_4Sb_3 structure and shows a comparable low thermal conductivity, casted doubts into the significance of structural disorder to low thermal conductivity [10]. Recently, peculiarities in the dynamic behavior—notably Einstein rattling of dumbbell units built from Sb atoms [11] and/or loosely bonded Zn atoms as evidenced from the superionic behavior of β-Zn_4Sb_3 [12,13]—have been put forward as possible reasons. It is not clear if these aspects would also apply to ZnSb. Furthermore, it should be noted that some ternary derivatives of zinc antimonides, like $Zn_5Sb_4In_{2-\delta}$ ($\delta \approx 0.15$), display similar low thermal conductivities as the binaries [14,15].

Zinc antimony compounds and their derivatives clearly have diverse crystal structures with features that individually could explain low thermal conductivity (e.g., presence of various forms of disorder, large sized unit cells). Yet, common to all systems is a covalent framework structure containing multicenter bonded structural entities. Peculiarities in the dynamic behavior could originate in the bonding properties of the framework structures; that is, multicenter bonded atoms may cause the incidence of pronounced anharmonic vibrational motion and/or give rise to localized low-energy optical modes (which couple with the acoustic, heat carrying phonons). The presence of localized low-energy optic modes as a consequence of multicenter bonded structural entities would provide a sound physical basis for the low thermal conductivity. This hypothesis has been put forward earlier [16], and recent theoretical investigations by Jund *et al.* [17] and Bjerg *et al.* [18] seem to confirm it.

The aim of the present paper is to shed more light on this issue. From heat capacity measurements, we reveal a great similarity of the vibrational properties of ZnSb and β-Zn_4Sb_3. From the analysis of the temperature dependence of the structural and atomic displacement parameters (ADPs), we find that Zn atoms display an increasingly anharmonic thermal motion at temperatures above 200 K. From phonon dispersion calculations and Raman spectroscopy, we consolidate the

*Present address: Department of Physics, Tsinghua University, Beijing 100084, China.

presence of low-energy optic modes in ZnSb as a consequence of multicenter bonded rhomboid ring entities Zn_2Sb_2. Those rings are also present in the structure of β-Zn_4Sb_3.

II. METHODS

A. Synthesis

Bulk samples of polycrystalline ZnSb were prepared from mixtures of zinc granules (ABCR, 99.99%) and antimony shots (ABCR, 99.999%) using a slight excess (2%) of Zn. Batches with a total mass between 0.5 and 1 g were loaded in fused silica tubes that were flame sealed in a dynamic vacuum ($<10^{-5}$ bar). The mixture of elements was melted with a torch while shaking the ampoule vigorously and then quenched in water. The obtained ingot was ground to a powder that was subsequently sealed in a fused silica tube and annealed for 5 days at 783 K. The obtained polycrystalline ZnSb was phase pure according to powder x-ray diffraction (PXRD) analysis. A part of the bulk sample was consolidated by spark plasma sintering (SPS) at 450 °C and 75 MPa for 5 min using a Dr. Sinter SCM 5000 instrument. In the following, we refer to this sample as the "SPS sample." Crystal specimens of ZnSb with sizes of several mm were prepared from reaction mixtures with 23 at.% Zn, 27 at.% Sb, and 50 at.% Bi, where Bi serves as a flux medium. Starting materials were Zn (granules, 99.99%), Sb (powder, 99.5%), and Bi (pieces, 99.999%). The procedure of crystal growth and separation is described in Ref. [6].

B. Powder x-ray diffraction

For PXRD analysis, the polycrystalline ZnSb bulk sample was finely ground. High temperature PXRD studies were performed on a Panalytical X'Pert PRO instrument with Cu Kα radiation in θ-2θ diffraction geometry. The powder sample was heated in dynamic vacuum ($\sim 10^{-5}$ bar) to 723 K using an Anton Paar XRK 900 chamber equipped with Be windows and connected to a temperature controller. Data in a 2θ range 10–60° were collected from 323 K in steps of 50 K, 100 min acquisition time, and 10°/min heating rate between the steps. Data collection was initiated when the temperature had stabilized. A RT diffraction pattern was collected on a Panalytical X'Pert Alpha1 diffractometer operated with Cu Kα_1 radiation, where the sample was mounted on a Si wafer zero-background holder. Rietveld refinement of PXRD data was performed using the Jana2006 package [19]. The details of the refinement results are given in the Supplemental Material [20].

C. Single crystal XRD

For single crystal XRD (SCXRD) analysis, crystals were selected among specimens obtained from flux synthesis. High resolution data were collected using a Bruker Smart Apex diffractometer equipped with a D8 goniometer and an Incoatec IμS Ag microsource ($\lambda = 0.56087$ Å) employing Helios mirror optics. Measurements were performed at several temperatures between 80 K and 400 K with an Oxford cryostream cooling unit. The frames were integrated with the Bruker SAINT software package [21] using a narrow-frame algorithm. A numerical, face-indexed absorption correction was applied using SADABS [22]. Data at 9 K were collected on a MAR345 imaging plate detector system with a rotating anode generator (Bruker FR591, $\lambda = 0.71073$ Å) using a displex cryosystem and a Huber 512.1 Eulerian cradle. The frames were integrated using the EVAL15 [23] software and a numerical absorption correction, and interframe scaling correction was performed using SADABS. Face indexing and crystal shape determination were, however, performed using the Smart Apex diffractometer. The EUHEDRAL [24] software was used to determine the crystal orientation during the measurements in the displex cryo-system for the subsequent numerical absorption corrections. All structure refinements were performed with Jana2006 [19]. All datasets were corrected for extinction (type 2) during the refinements. In order to exclude a possible bias between the correction of absorption and extinction effects, which mainly affect the data at low resolution, ADP values were also derived from refinements of high order Bragg reflection ($\sin\Theta/\lambda > 0.6$ Å^{-1}). However, the ADP values derived independently from both methods did not differ significantly. The details of refinement summary and parameters are given in the Supplemental Material [20].

D. Raman spectroscopy

Raman spectroscopy investigations were performed on ZnSb crystal specimens obtained from flux growth and on a disk-shaped specimen with 12 mm diameter obtained from SPS consolidation. For comparison, elemental Sb (as purchased) was also investigated. Raman spectra were measured using a Labram HR 800 spectrometer. The instrument is equipped with an 800 mm focal length spectrograph and an air cooled (−70 °C), back thinned charge-coupled device (CCD) detector. Samples were excited using an air cooled double frequency Nd:YAG laser (532 nm) with a reduced input laser power of 0.56 mW and an air cooled intracavity regulated laser diode (785 nm) with a reduced laser power of 0.88 mW. Raman spectra were collected with an exposure time of 60 s, accumulation number of 10, and using an 1800 grooves/mm grating.

E. Heat capacity measurements

For heat capacity measurement, a crystal specimen (14.8 mg) and a SPS sintered piece (28.0 mg) were used. The heat capacity was measured between 2 K and 290 K (49 points distributed logarithmically) and between 330 K and 400 K in 3 K increments using a quasiadiabatic step heating technique, as implemented in the Physical Property Measurement System (PPMS) by Quantum Design. The samples were thermally connected to the platform of the sample holder via a small amount of Apiezon-N grease for $T < 300$ K and Apiezon-H for $T > 300$ K (both typically 0.1–0.3 mg). The uncertainty for this measurement technique is estimated to be lower than 5%.

F. Computation

The phonon dispersion relations and thermodynamic functions of ZnSb were calculated via the ABINIT program package [25–27] and employed the generalized gradient approximation (GGA) with the Perdew-Burke-Ernzerhof (PBE) parameterization [28,29]. The GGA-PBE pseudopotentials

were provided by the ABINIT website. These pseudopotentials are norm conserving and were generated using the fhi98PP package [30]. A 6 × 6 × 6 Monkhorst-Pack [31] k-point grid was used for electronic integration, and a 2 × 2 × 2 q-grid was used for calculations of the dynamical matrix elements. A plane wave energy cutoff of 35 Hartree (∼950 eV) was employed. Prior to the phonon dispersion calculations, ZnSb was relaxed with respect to lattice parameters and atomic positions with forces converged to better than 1×10^{-3} eV/Å. From the phonon density of states (PDOS), it is possible to obtain the thermodynamic functions of a material [32]. Within the harmonic approximation, the contribution from the phonons per unit cell to the internal energy ΔE, the Helmholtz free energy $\Delta F = \Delta E - TS$, the constant volume specific heat C_v, and the entropy S, at temperature T are given by

$$\Delta F = 3nk_BT \int_0^{\omega_L} \ln\left\{2\sinh\frac{\hbar\omega}{2k_BT}\right\} g(\omega)d\omega \quad (1)$$

$$\Delta E = 3n\frac{\hbar}{2}\int_0^{\omega_L} \omega\coth\left(\frac{\hbar\omega}{2k_BT}\right) g(\omega)d\omega \quad (2)$$

$$C_v = 3nk_B\int_0^{\omega_L}\left(\frac{\hbar\omega}{2k_BT}\right)^2 \mathrm{csch}^2\left(\frac{\hbar\omega}{2k_BT}\right) g(\omega)d\omega \quad (3)$$

$$S = 3nk_B\int_0^{\omega_L}\left[\frac{\hbar\omega}{2k_BT}\coth\frac{\hbar\omega}{2k_BT} - \ln\left\{2\sinh\frac{\hbar\omega}{2k_BT}\right\}\right] g(\omega)d\omega, \quad (4)$$

where k_B is the Boltzmann constant, ω is the phonon frequency, ω_L is the largest frequency, n is the number of atoms in the unit cell, $g(\omega)$ is the PDOS, and csch is the hyperbolic cosecant.

The ADPs can be obtained from the PDOS with the knowledge of the corresponding eigenvectors $e^l_{n\alpha}(\vec{q})$ and the partial DOS of the phonons. The partial DOS of the phonons is given by [33]

$$g_{n\alpha\beta}(\omega) = \sum_{\vec{q},l}\delta(\omega-\omega_l(\vec{q}))\left\langle e^{l*}_{n\alpha}(\vec{q})e^l_{n\beta}(\vec{q})\right\rangle, \quad (5)$$

where α and β represent the x, y, or z Cartesian coordinates, n is the atom index, l is phonon mode, and $\vec{q}$ is the wave vector in the Brillouin zone. The ADPs U_{nij} are calculated as

$$B_{n\alpha\beta} = \int_0^{\infty}\frac{8\pi^2\hbar}{M_n\omega}g_{n\alpha\beta}(\omega)\left(\frac{1}{\exp\left(\frac{\hbar\omega}{k_BT}\right)-1}+\frac{1}{2}\right)d\omega, \quad (6)$$

with

$$U_{nij} = \frac{1}{8\pi^2}\sum\frac{b_{i\alpha}B_{n\alpha\beta}b_{j\beta}}{|\vec{b}_i||\vec{b}_j|}, \quad (7)$$

where M_n is the mass of atom n and $\vec{b}_i$ $(i, j = 1, 2, \text{or } 3)$ are the crystal reciprocal lattice vectors. U_{nij} is a tensor that defines the average motions of the atoms within the compounds (with dimensions of length squared). The isotropic ADPs U^n_{iso} can be derived directly from the anisotropic U_{nij} values by

$$U^n_{\text{iso}} = \frac{1}{3}\sum_i U_{nii}. \quad (8)$$

III. RESULTS AND DISCUSSION

A. Temperature dependent structural properties and thermal stability

ZnSb crystallizes with an orthorhombic *Pbca* structure (the CdSb type) that contains eight formula units in the unit cell [34]. Both kinds of atoms are situated on the general position 8*c*. The structure may be described as being built from rhomboid rings Zn_2Sb_2, which are arranged in layers and linked to 10 neighboring rings. Figure 1(a) shows the arrangement of layers along the [001] direction. (Note, that because of the three axial glides, this description holds for any direction.) In a layer, each ring is surrounded by six neighboring ones: two are attached to each Sb atom and one to each Zn atom of one Zn_2Sb_2 moiety. Additionally, each atom will then bind to a ring in an adjacent layer. As a result, Zn and Sb atoms in the ZnSb structure attain a peculiar fivefold coordination by one like and four unlike neighbors [Fig. 1(b)]. A ring and its linkage to neighboring ones is shown in Fig. 1(c).

According to Refs. [35] and [36], the rhomboid ring represents a four center, four electron (4*c*4*e*) bonded entity, which is connected via 2*c*2*e* bonds to the 10 neighboring ones. This bonding model provides an electron precise situation for ZnSb. There are six distinct nearest neighbor distances in the ZnSb structure, which are all captured within the rhomboid ring and its connectivity [cf. Fig. 1(c)]. The different bonding motifs (rhomboid ring multicenter 4*c*4*e* and connecting 2*c*2*e* bonds) can be recognized in the distribution of interatomic

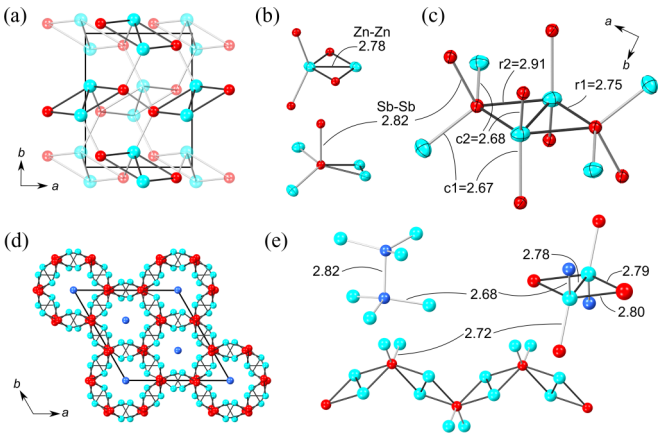

FIG. 1. (Color online) (a) The orthorhombic crystal structure of ZnSb built from layers (dark and pale colors) of rhomboid rings Zn_2Sb_2. Cyan and red balls denote Zn and Sb atoms, respectively. (b) Local five-coordination of Zn and Sb atoms. The inserted numbers indicate interatomic distances in Angstroms at room temperature. (c) Rhomboid ring Zn_2Sb_2 and its connectivity to neighboring rings. Distances are distinguished as c (connecting) and r (ring) types. The center of a ring corresponds to a center of inversion. The thermal ellipsoids correspond to 90% probability density at room temperature obtained from SCXRD measurements. (d) Idealized Zn_6Sb_5 framework of rhombohedral β-Zn_4Sb_3 along the [001] direction. The framework is built from chains of condensed rhomboid rings $Zn_2Sb1_{2/2}$ [cf. panel (e)] and consists of channels that are stuffed by Sb2 atoms (depicted as blue balls). Sb2-Zn bonds are omitted for clarity. (e) Structural fragments and local coordination of Zn, Sb1, and Sb2 atoms in β-Zn_4Sb_3.

distances: Zn-Sb interatomic distances within a ring (r-type distances) are about 0.1 Å larger than the ring connecting ones (c-type distances). The short Zn-Zn distance (2.78 Å) is part of the multicenter bonding motif, while the short Sb-Sb distance of around 2.82 Å corresponds to a ring-linking $2e2c$ bond. These nearest neighbor distances associated with bonding interactions are well separated from the next nearest ones, starting off above 3.5 Å. To further support the $4c4e$ bonding picture for ZnSb, we performed a topological analysis of the electron density using the full-potential linearized augmented plane wave (FP-LAPW) Elk code [37] and DGrid 4.6 [38]. Details are given in Supplemental Material S8 [20]. We note that among the r-type distances, $r2$ is considerably longer than $r1$. This is reflected in lower electron density values at the bond critical points (BCP) for $r2(\rho_{\mathrm{BCP},r2} = 0.222\,\mathrm{e/Å^3})$, which is also lower than the electron density at the BCP for $r1(\rho_{\mathrm{BCP},r1} = 0.304\,\mathrm{e/Å^3})$. The weakest, although not the shortest, bond is the Zn-Zn bond ($\rho_{\mathrm{BCP,Zn-Zn}} = 0.183\,\mathrm{e/Å^3}$), in accordance with the proposed bonding picture. The electron density in the bonding region of the Zn_2Sb_2 moiety is very flat, nevertheless the ring critical point ($\rho_{\mathrm{RCP}} = 0.178\,\mathrm{e/Å^3}$) of the Zn_2Sb_2 rhomboid ring is well separated from all BCPs in the ring. Therefore, we consider all Zn-Sb bonds in the Zn_2Sb_2 moiety as topologically stable bonds due to the presence of distinct BCPs. Importantly, electron poor multicenter bonding is clearly signaled by endocyclic bondpaths and high ellipticity values of the electron density at the BCPs [39,40].

The rhomboid ring Zn_2Sb_2 motif is also the central feature of the β-Zn_4Sb_3 structure [Fig. 1(d)] [16,36]. Here rings are condensed into chains by sharing common Sb atoms [Fig. 1(e)]. These Sb atoms (termed Sb1) then attain a six coordination by Zn atoms by connecting with two neighboring chains via $2c2e$ bonds. The linkage of chains in the final framework is completed by additional Sb atoms (termed Sb2) forming dumbbells [Fig. 1(e)]. Each dumbbell unit has six chain-linking Sb2-Zn contacts, also corresponding to $2c2e$ bonds, while the Sb2 atoms are tetrahedrally coordinated. We emphasize that "dumbbells" of Sb atoms also occur in the ZnSb structure; however, in ZnSb they correspond to direct links of neighboring rhomboid rings, and their coordination environment is rather different from the one in β-Zn_4Sb_3.

To investigate the effect of temperature to the structural parameters of ZnSb we performed SCXRD measurements from 9 to 400 K and PXRD measurements from RT up to 723 K. Figures 2(a) and 2(b) show lattice parameters and unit cell volume as a function of temperature, respectively. Lattice parameters refined from PXRD data are more accurate. They increase linearly in the range 300–675 K. The RT volume expansion coefficient $\alpha_V(300\ \mathrm{K})$ is estimated as $4.15 \times 10^{-5}\ \mathrm{K^{-1}}$, which is comparable to many metals (e.g., Cu: $5.1 \times 10^{-5}\ \mathrm{K^{-1}}$; Au: $4.2 \times 10^{-5}\ \mathrm{K^{-1}}$). We note noticeable anisotropy of the RT linear thermal expansion coefficients for the individual lattice parameters: $\alpha_c = 0.404 \times 10^{-5}\ \mathrm{K^{-1}}$, $\alpha_b = 1.25 \times 10^{-5}$ K, and $\alpha_a = 2.45 \times 10^{-5}$ K. The ratio $\alpha_c : \alpha_b : \alpha_a$ corresponds roughly to 1:3:6. The variation of interatomic distances obtained from the refinement of the SCXRD data is shown in Fig. 2(c) in the range of 9–400 K. Two of the six nearest neighbor distances show pronounced temperature variation: the intraring distances $r2$ and the Zn-Zn

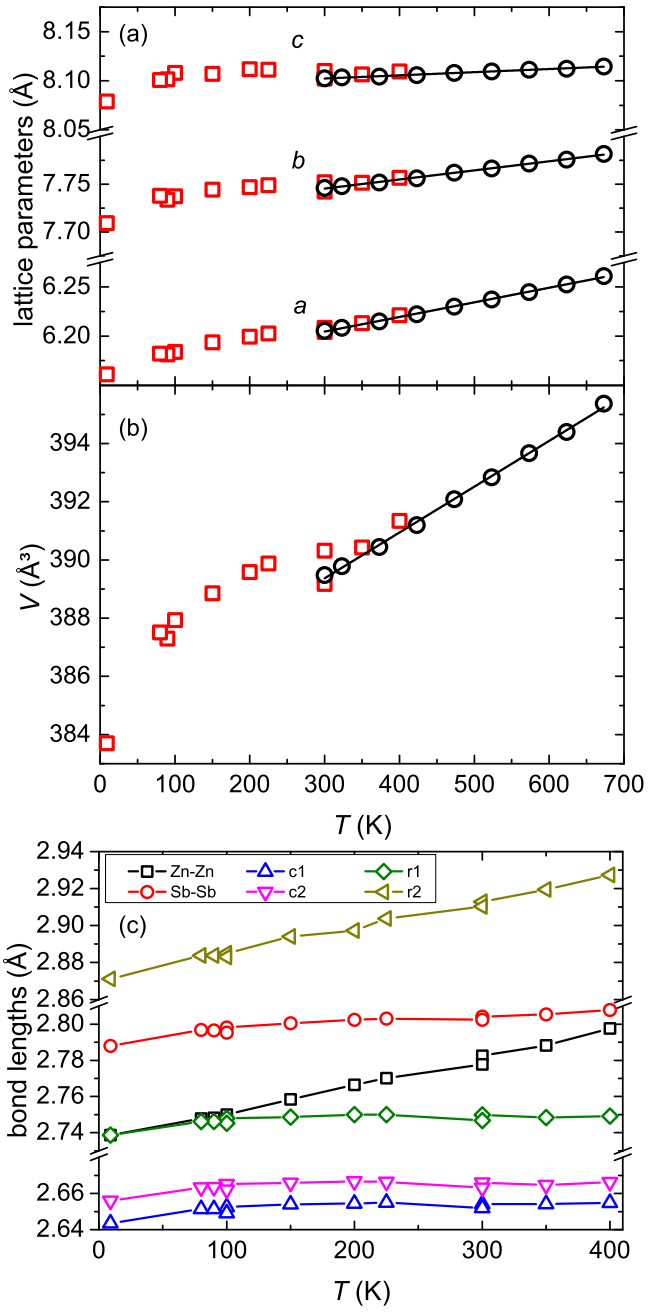

FIG. 2. (Color online) (a) Lattice parameters and (b) unit cell volume of ZnSb as a function of temperature. Squares and circles denote parameters obtained from SCXRD and PXRD refinements, respectively. The solid line represents a linear fit to the PXRD data. (c) Variation of interatomic distances in ZnSb as a function of temperature. Data were obtained from refinements of SCXRD data including anharmonic atomic displacement parameters (using a Gram-Charlier expansion). For the assignment of the individual bond lengths, see Fig. 1. The size of the symbols used in panels (a)–(c) exceeds by far the standard deviation of the corresponding data point.

separation increase roughly linearly from 2.87 to 2.93 Å and from 2.74 to 2.80 Å with increasing temperature from 9 to 400 K, respectively. The remaining distances increase in the same temperature range only by 0.01 to 0.015 Å, corresponding to a change of 0.4–0.5%.

As initially mentioned, ZnSb possesses only one crystallographic independent Sb and Zn atom per asymmetric unit. Temperature variation from 9 to 400 K mainly affects the atomic coordinates of the Zn atom, whereas the the Sb atom position is hardly affected. As a consequence, the increase of the long Zn-Sb distances [denoted $r2$ in Fig. 1(c)] with increasing temperature is strongly correlated with a simultaneous elongation of the Zn-Zn distances. In contrast, the shorter Zn-Sb bonds ($r1, c1, c2$) appear to be characterized by stronger force constants and expand only moderately with increasing temperature. The significant increase of the long Zn-Zn and Zn-Sb distance within the Zn_2Sb_2 moieties may therefore be regarded as a weakening of the multicenter bonding that could parallel the onset of the thermal decomposition of ZnSb (see below).

Figure 3 shows the PXRD patterns of ZnSb upon heating between 300 and 723 K in a dynamic vacuum. At 573 K, the onset of the sample decomposition is signaled by the occurrence of reflections of elemental antimony. Phase analyses by Rietveld refinements yield an amount of elemental Sb of 1.4(2) wt%. At 723 K (and about 5 h after the 573 K measurement), the ZnSb sample is almost completely decomposed. The Sb phase fraction increased to 78.4(4) wt%. The presence of dynamic vacuum conditions clearly promotes the decomposition of ZnSb (into elemental Sb and Zn vapor), which otherwise, according to the Zn-Sb phase diagram [41], represents a thermodynamically stable phase up to at least 800 K. The same phenomenon has been observed for β-Zn_4Sb_3: Heating Zn_4Sb_3 in a dynamic vacuum leads to the formation of ZnSb at 623 K, which in turn decomposes above 693 K [42]. Thus, the thermal stability of ZnSb and β-Zn_4Sb_3 under dynamic vacuum conditions is comparably low.

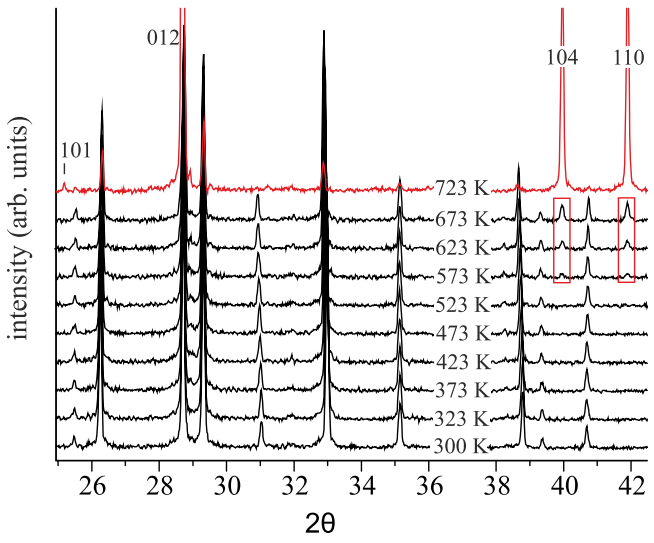

FIG. 3. (Color online) PXRD patterns (Cu Kα radiation) of the ZnSb bulk sample at temperatures between 300 and 723 K in a 2Θ range of 25–42.5°. At 573 K, reflections from elemental antimony occur (marked with boxes). At 723 K, the sample decomposition is already severe, and a mixture of ZnSb and elemental Sb ($R\bar{3}m$) with a molar ratio of approximately 1:6 is observed. Bragg reflections of the Sb impurity phase are marked by their corresponding Miller indices.

B. Heat capacity measurements

Heat capacity studies of ZnSb have been performed already in the 1970s by Mamedova *et al.* [43] and Danilenko *et al.* [44]. The key results of these studies are compared to our studies in Fig. 4. The measurement of Danilenko *et al.* [44] exceeds the Dulong-Petit limit of $C_v = 3R$ per mole and atom (49.9 J/mol-K for ZnSb) at temperatures above 240 K. A similar behavior is also displayed by our SPS sample, whereas our crystalline sample reaches this limit just above 330 K, in better agreement with the results of Mamedova *et al.* [43] (especially below 120 K), whose ZnSb sample actually contained 3 wt.% CdSb. The higher C_p values for the SPS sample may be explained by defects or stress/strain introduced by the SPS consolidation process.

As a next step, we attempted to describe the C_p data by a simple Debye-Einstein model, which assumes a Debye-type behavior for the three acoustic phonon branches and an Einstein (independent oscillator) behavior for the contributions from the optical branches [45]. Additionally, a linear expansion coefficient A_1 is employed to account for the volume dependence of C_p in the high temperature range. The model (in the following referred as "model 1") used can be expressed by the equation:

$$C_v(T) = 3R\left(D(T,\Theta_D) + \sum_{i=1}^{k} c_i E_i(T,\Theta_{E,i})\right)$$
$$C_v(\infty) = 3nR, \tag{9}$$

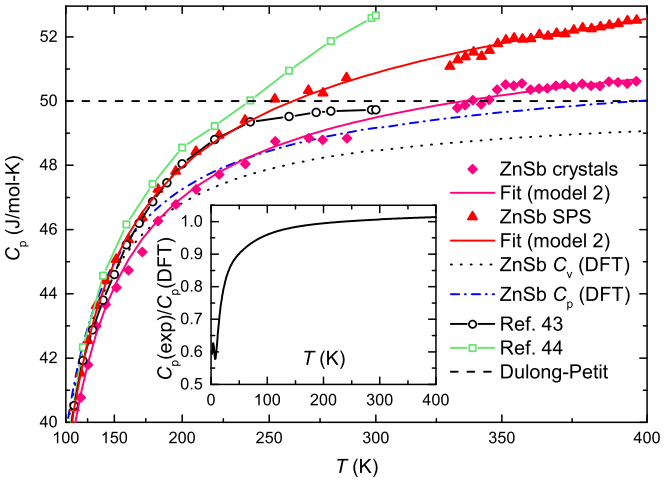

FIG. 4. (Color online) Temperature dependent heat capacity $C_p(T)$ (per formula unit) of crystalline and SPS consolidated ZnSb samples (pink diamonds and red triangles, respectively) and their corresponding fits (model 2) as pink and red solid lines, respectively. The Dulong-Petit limit of $3R$ is marked as a black broken horizontal line. Earlier measurements of Danilenko *et al.* [44] and Mamedova *et al.* [43] have been added for comparison (black circles and green squares, respectively; interconnection lines are a guide for the eye). DFT calculated heat capacities C_v and C_p of ZnSb are shown as dashed black and dashed-dotted blue lines, respectively. The theoretical C_p values have been estimated via the thermal expansion coefficient from the PXRD measurements (see below). The inset shows the ratio of experimental and theoretical C_p values.

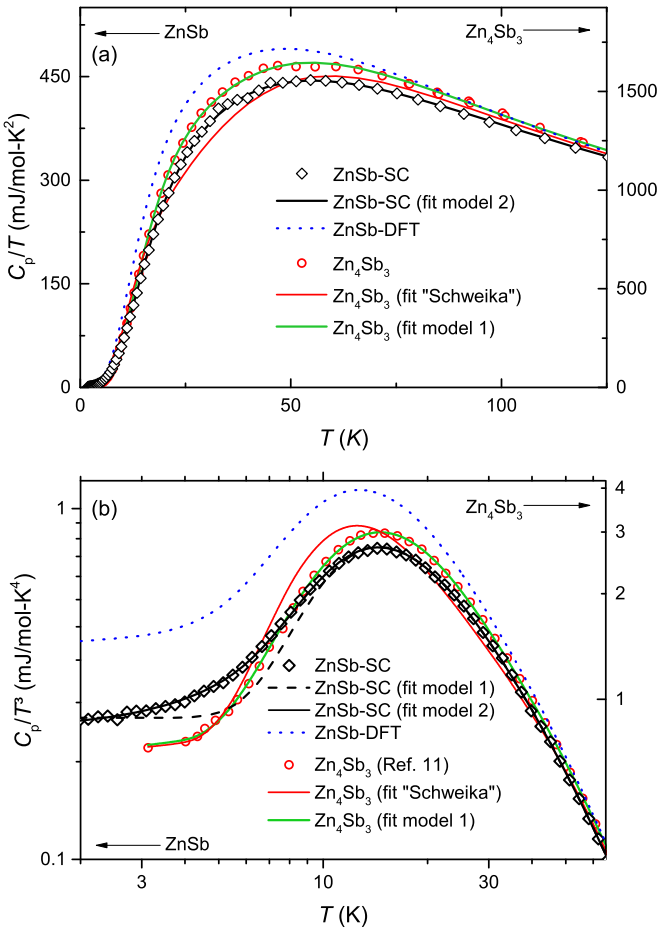

FIG. 5. (Color online) (a) Heat capacity C_p/T (per formula unit) of ZnSb (black diamonds) including Debye-Einstein fit (model 2, solid black line) and Zn_4Sb_3 (red circles) including the original fit of Schweika *et al.* [11] (solid red line) as well as the improved fit using model 1 (solid green line). The DFT calculated data of ZnSb is shown as a dotted blue line. (b) C_p/T^3 (per formula unit) representation of panel (a) with additional fit for ZnSb (model 1, dashed black line) for comparison. The y axis range is scaled according to the number of atoms per formula unit in ZnSb and Zn_4Sb_3 by the ratio 2:7 for both C_p/T and C_p/T^3.

where D is the temperature dependent Debye contribution, E_i the temperature dependent Einstein contributions, c_i their respective coefficients, and n the number of atoms per formula unit. The quasiharmonic (QH) approximation of C_p can then be described as

$$C_p(T) = C_v(T)(1 + \tilde{C}_v(T)\, A_1 T) \quad \tilde{C}_v(T) = \frac{C_v(T)}{C_v(\infty)}. \quad (10)$$

The Debye contribution was fixed to $3R$, whereas the contributions of the Einstein terms were refined individually but constrained to a sum of $3R$ in order to fulfill the Dulong-Petit law. This simplistic model (model 1) using one Debye and two Einstein components ($E_1 + E_2$) produced a highly satisfactory fit [Fig. 4 and Fig. 5(a)], apart from the region at very low temperatures {below 10 K, which is also characterized by nonconstant C/T^3 values [Fig. 5(b)]}.

The latter observation indicates deviations from a pure Debye behavior at low temperatures [only ω^2 dependence of the PDOS; $g(\omega) \sim \omega^2$ in Eq. (3)]. Additional quartic [$g(\omega) \sim \omega^4$] contributions are, however, frequently observed in binary II-VI or III-V semiconductors [46]. We therefore included such a non-Debye (ND) component [model 2, Eq. (11)] in our specific heat capacity model of ZnSb. For stability reasons, Θ_{ND} was set in the fitting procedure to the lowest Einstein temperature Θ_{E1}, as suggested by others [47], and the sum of the Debye and ND components was constrained to $3R$,

$$C_v(T) = 3R\Big(c_D D(T,\Theta_D) + c_{ND} N D(T,\Theta_{ND}) + \sum_{i=1}^{k} c_i E_i(T,\Theta_{E,i})\Big); \quad (11)$$
$$c_D = (1 - c_{ND}).$$

The fits are detailed in Figs. 5(a) and 5(b) as C_p/T and C_p/T^3 plots, respectively. The more sophisticated model 2 (black solid line) improves the fit of the C_p for ZnSb in the low temperature regime of 3–10 K, significantly in comparison with model 1 [dashed black line, cf. Fig. 5(b)]. This stresses the necessity to consider a ND component for a precise description of the temperature dependence of C/T^3 in this temperature regime. The Debye temperature $\Theta_D(0)$ of ZnSb is obtained as 248 K from the slope of C/T vs T^2 representation for $T < 3$ K. Jund *et al.* [17] calculated the Debye temperature of ZnSb from averaged sound velocity data measured by Balazyuk *et al.* [48] and obtained a value of 253 K, which is in close agreement with our findings. The fitted Einstein temperatures $\Theta_{E1} = 77.6$ K (54 cm^{-1}, 6.7 meV) and $\Theta_{E2} = 276.9$ K (192 cm^{-1}, 23.9 meV) refer to the single crystal sample. The results of the fit of the SPS sample data with Eqs. (9) and (10) are very similar. The according coefficients are listed in Table I.

Bjerg *et al.* [18] recently reported Debye temperatures that were derived from the density functional theory (DFT)-calculated heat capacity of ZnSb employing the Slack definition. The value specified for ZnSb ($\Theta_{D,Slack} = 92$ K) appears to be significantly lower than the experimental value of this paper, which is derived from heat capacity measurements using a Debye-Einstein model ($\Theta_{D,Cp} = 248$ K), see above and Table I. The seemingly large difference, however, is simply due to the fact that Bjerg *et al.* [18] specified a reduced Debye temperature of 92 K in their theoretical DFT study. According to the Slack definition, the reduced Debye temperature depends on the number of atoms n ($n = 16$ for ZnSb) in the primitive unit cell and can be converted to conventional Debye temperatures by multiplying the reduced value with $n^{(-1/3)}$, which yields a Debye temperature of 232 K, in close agreement with our experimental value [49,50].

We further note that the theoretical study by Jund *et al.* [17] derived a value of 209.3 K for the Debye temperature $\Theta_D(0)$, which again agrees very well with our theoretical findings ($\Theta_D(0) = 210$ K).

The temperature dependence of the heat capacity of ZnSb and Zn_4Sb_3 is highly related. This is shown in Fig. 5(a) where our measurement for single crystalline ZnSb is compared with the heat capacity of polycrystalline Zn_4Sb_3, as obtained by Schweika *et al.* [11]. The authors described the heat capacity of Zn_4Sb_3 by a model containing only one Debye and one Einstein contribution with a ratio of 85:15. The energy

TABLE I. Coefficients obtained from fits of the experimental heat capacity of ZnSb and Zn_4Sb_3 using the models described above.

	ZnSb-SC	ZnSb-SC	ZnSb-SPS	ZnSb-calc	Zn_4Sb_3[a]	Zn_4Sb_3[b]
model	1	2	2	2	1	Schweika
$\Theta_D(0)$ [K]	248	248	253	210	251	240
Θ_D [K]	197.3	195.2	200.5	167.0	137.9	251
c_D [atoms]	1	0.90	0.93	0.95	1	5.95
Θ_{ND} [K]	-	77.6[c]	77.0[c]	64.5[c]	-	-
c_{ND} [atoms]	-	0.10	0.07	0.05	-	-
Θ_{E1} [K]	71.5	77.6[c]	77.0[c]	64.5[c]	56.2	62
c_{E1} [atoms]	0.36	0.30	0.34	0.29	0.38	1.05
Θ_{E2} [K]	285.7	276.9	271.8	257.0	221.0	-
c_{E2} [atoms]	0.64	0.70	0.66	0.71	4.01	-
Θ_{E3} [K]	-	-	-	-	85.4	-
c_{E3} [atoms]	-	-	-	-	1.60	-
A_1 [$10^{-6}K^{-1}$]	95.2	93.6	187.4	49.9	76.7	-

[a]Data from Ref. [11].
[b]Original fitting model (three parameter, two component fit) by Schweika *et al.* [11].
[c]Constrained.

of the Einstein mode was very low (5.4 meV, 62 K) and associated with a physical oscillator in the Zn_4Sb_3 structure, i.e., the aforementioned rattling of Sb_2 dumbbells. However, the Schweika *et al.* [11] model is physically implausible because the majority of optical modes would be assigned a Debye behavior. As a matter of fact, this simple model displays significant discrepancies to the experimental data, especially in the low temperature regime ($T < 125$ K), as shown in Figs. 5(a) and 5(b). To obtain a proper fit using a Debye-Einstein model similar to ZnSb (model 1), one Debye and three Einstein terms (E_1, E_2, E_3) are needed [cf. Figs. 5(a) and 5(b)]. The coefficients are presented in Table I. As for ZnSb, the Debye contribution was fixed to $3R$, whereas the contributions of the Einstein terms were refined individually. Due to the presence of a phase transition in Zn_4Sb_3, data around 250 K were excluded. The necessity of ND contributions was not justified for Zn_4Sb_3.

The fitted Einstein temperatures for Zn_4Sb_3 are $\Theta_{E1} = 56.2$ K (39 cm^{-1}, 4.8 meV), $\Theta_{E2} = 221.0$ K (153 cm^{-1}, 19.1 meV), and $\Theta_{E3} = 85.4$ K (59 cm^{-1}, 7.4 meV). Accordingly, our model (model 1) uses two low-energy Einstein modes as compared to one in the Schweika *et al.* [11] model. The ratio of low- and high-energy Einstein mode contributions $(c_{E1} + c_{E3}):c_{E2}$ is about 1:2, which is similar to the ratio $c_{E1}:c_{E2}$ for ZnSb. Also the Debye temperature $\Theta_D(0)$ at low temperatures of both compounds is very similar (around 250 K). We conclude that although the fitting equations for the heat capacity of ZnSb and Zn_4Sb_3 were somewhat different, their overall temperature dependence is very similar. This indicates that both compounds are characterized by rather similar lattice dynamical and thermal properties.

C. Lattice dynamics and vibrational properties

Figure 6(a) shows phonon dispersion curves obtained from first principles calculations and the corresponding PDOS of ZnSb. There is good agreement between our linear response-based calculations and the calculations by Jund *et al.* [17] and Bjerg *et al.* [18], employing a methodology using a super cell approach. The prominent feature of the PDOS is the occurrence of a gap between 125 and 140 cm^{-1}. This gap separates 20 modes of high energies from the remaining ones. The high-energy modes appear to be split into a 4 + 4 (in the range 170−190 cm^{-1}) and 8 + 4 pattern (in

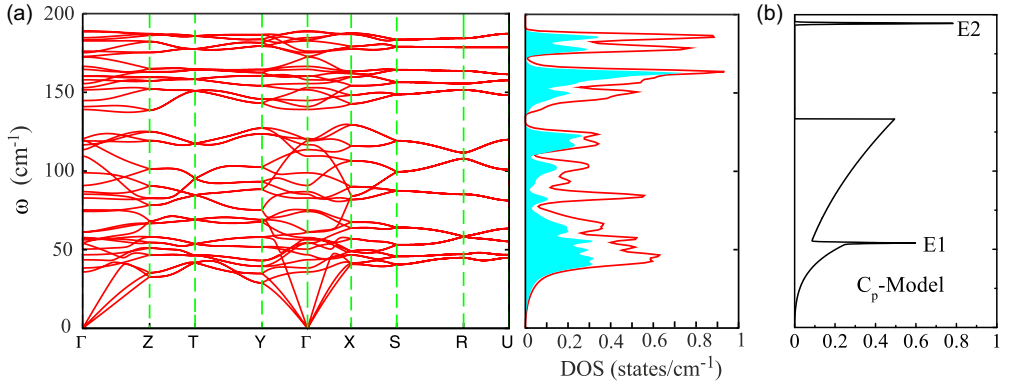

FIG. 6. (Color online) (a) Calculated phonon dispersion curves (left) and PDOS of ZnSb (right). The partial Sb atom contribution to the PDOS is indicated by the cyan area. (b) PDOS model based on the Debye and Einstein temperatures as extracted from the measured heat capacity. (c) PDOS constructed from fitting model 2 (cf. Table I).

the range 140−170 cm^{-1}). We note that the magnitude of atomic displacements of the Zn and Sb atoms with regard to the individual normal modes of vibration is rather similar, despite their large mass difference. However, some exceptions are observed. Weakly dispersed modes at around 165 cm^{-1} and 145 cm^{-1} are characterized by large displacements of the Sb and Zn atoms, respectively. The mode at 165 cm^{-1} may be associated with the stretching mode of Sb_2 moieties (note that this is not a "dumbbell rattling" mode). Among the low-energy modes (below the gap), the ones around 83 cm^{-1} are distinguished because of their weak dispersion and their characteristic and predominant Zn displacements. Last, we note an accumulation of low-energy optic modes with small dispersion in the range between 35 and 60 cm^{-1}, which conforms with the earlier calculations of Jund *et al.* [17] and Bjerg *et al.* [18].

Figure 6(b) shows the model PDOS reconstructed from the experimental specific heat data of ZnSb using model 2 (cf. Table I). Both Einstein temperatures are well reflected in the theoretical PDOS: Θ_{E1} (276.9 K) accounts for the presence of 20 high-energy modes above the gap and Θ_{E2} (77.6 K) partially accounts for the accumulation of low-lying optical modes. The acoustic modes and part of the low-lying optical modes are described by the Debye and ND contributions of model 2 (Table I). Hence, the proposed Debye-Einstein model appears to be physically reasonable, also in comparison with the theoretical PDOS.

To probe the optic modes of ZnSb, we performed Raman spectroscopy on single crystal and SPS consolidated specimens. The orthorhombic structure with eight formula units gives rise to 24 Raman active A_g, B_{1g}, B_{2g}, and B_{3g} modes; 15 infrared (IR) active B_{1u}, B_{2u}, and B_{3u} modes; and 6 silent A_u modes. Earlier Raman studies claimed the detection of 16 modes [51,52]. However, most bands were very broad, and some were very weak. It appears doubtful whether 16 modes were really detected. Furthermore, their assignment is very difficult because of the similar wave numbers. The general features of the Raman spectrum of ZnSb are an asymmetric band with high intensity at around 173 cm^{-1} and several weak and broad bands below 80 cm^{-1}. This overall appearance was confirmed more recently by Trichês *et al.* [53].

Our spectra are compiled in Fig. 7 and compared with the experimental spectrum of elemental Sb and the theoretical wave numbers of the Raman active modes obtained from first principles calculations. Rhombohedral Sb displays two Raman active modes: the A_g mode at 150 cm^{-1}, which is characterized by Sb atoms shifting along the C_3 axis, and the degenerate E_g band at 110 cm^{-1}, which triggers the displacement of atoms perpendicular to the C_3 axis. We note that the stretching mode of Sb_2 moieties in ZnSb occurs at higher wave numbers (ca. 165 cm^{-1}). Compared to the previous measurements [48,51,52], our spectra display a lower signal to noise ratio and a higher resolution. Excitation with a green laser ($\lambda = 532$ nm) yields spectra that are characterized by a prominent band at 173 cm^{-1}. However, in contrast with the earlier measurements [48,51,52], this band is now clearly split into two components (173 cm^{-1} and 177 cm^{-1}). Further bands are consistently observed at ca. 200 cm^{-1}, 75−80 cm^{-1}, and 50−55 cm^{-1}. Spectra from single crystal specimens display additional bands at ∼100, ∼130, and ∼145 cm^{-1}. We note

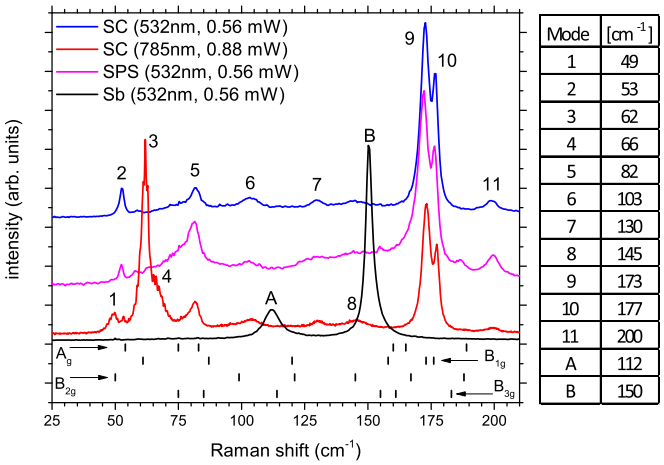

Mode	[cm^{-1}]
1	49
2	53
3	62
4	66
5	82
6	103
7	130
8	145
9	173
10	177
11	200
A	112
B	150

FIG. 7. (Color online) Raman spectrum of ZnSb and elemental antimony recorded with an excitation wavelength of 532 nm and 785 nm. The listed values on the right-hand side are given in wave numbers (cm^{-1}) for the labeled bands 1–11 for ZnSb and A-B for elemental antimony. The wave numbers of the individual optical modes were obtained from the DFT calculation at the Γ point and are shown as bars at the bottom of the spectra.

that the location of bands may vary by 1−3 cm^{-1} in different spectra due to the local heating of the sample by the laser beam. In spectra obtained from red laser excitation ($\lambda = 785$ nm), the low-energy modes become more pronounced. In addition to the occurrence of a band at 49 cm^{-1}, we observe an additional intense band at around 62 cm^{-1} with a characteristic shoulder at 66 cm^{-1}. The latter band could not be observed when the green laser excitation ($\lambda = 532$ nm) was used instead. We further stress that it is important to excite the sample with a low laser power (0.56 mW, corresponding to a power density of approx. 5.5 × 10^{-5} $mW/\mu m^2$). At higher laser powers, bands at around 150 and 110 cm^{-1} appear, which signal the formation of elemental Sb and thus the onset of a thermally induced decomposition of ZnSb in the laser beam.

In summary, our Raman investigation revealed up to 10 distinct bands in the range from 50 to 200 cm^{-1} and unequivocally revealed the presence of low-energy optic modes at around 50 cm^{-1}. Calculated wave numbers for Raman active modes appear to be underestimated by 5–10%. Smirnov *et al.* [51] also characterized the IR modes of ZnSb from reflectivity spectra and magnetophonon resonance data. These IR modes were found in the ranges 184−195 cm^{-1}, 155−166 cm^{-1}, 119−123 cm^{-1}, and 44−66 cm^{-1}.

With the knowledge of the PDOS of ZnSb, the theoretical vibrational heat capacity at constant volume (C_v) can be calculated according to Eq. (3) (cf. Fig. 4 and Fig. 5). Following the analysis by Jund *et al.* [17], a linear term $A_1 = A_1^{QH} + A_1^{anh}$ may be added to the harmonically calculated $C_v(T)$ values [cf. Eq. (11)] to account for the QH volume change and anharmonic contributions, respectively (denoted as A and B in Ref. [17], respectively). The value of A_1^{QH} can be approximated as $(B_M V \alpha_v^2 / C_{v,\infty})$, where B_M is the bulk modulus, V is the molar volume, and α_v is the volume expansion coefficient. A_1^{QH} is then obtained as 49.9 × 10^{-6} K^{-1} using values of B_M from the literature ($B_M \sim 50$ GPa [17,48,53]) and values of V and

α_v^2 from this paper. The correction term $A_1 = A_1^{QH}$ was then applied to calculate C_p (cf. Fig. 4). Figure 4 clearly reveals that in the high temperature range, the experimental $C_p(T)$ values are slightly larger than the theoretical C_p values [note that the A_1 parameters obtained from the Debye-Einstein fitting are substantially higher (cf. Table I)]. For the single crystal C_p data, we attribute this discrepancy to anharmonicity (the corresponding value for A_1^{anh} would then be 43.7×10^{-6} K^{-1}), whereas for the SPS sample defects, stress or strain may provide additional contributions. We can exclude significant impurity contributions of the SPS sample since the PXRD pattern after SPS sintering did not show any additional peaks (see Supplementary Material Fig. S7 [20]).

Below $T = 150$ K, the calculated C_p values are higher than the experimental C_p values. This deviation becomes even more pronounced with decreasing temperature (see inset in Fig. 4). This discrepancy is primarily attributed to an underestimation of the calculated phonon frequencies (as indicated from the comparison of calculated Raman modes and measured bands). At these low temperatures, underestimated phonon frequencies will lead to an overestimation of the heat capacity. Due to the asymptotic nature of C_v with respect to the Dulong-Petit limit, this discrepancy is only of minor importance at elevated temperatures. As a consequence, the Debye and Einstein temperatures obtained from a fit of the calculated $C_p(T)$ data to a Debye-Einstein model (model 2) are considerably lower compared to the values of the experimental C_p data (cf. Table I).

In order to investigate in greater detail the nature of normal modes of vibrations in ZnSb, we examined the temperature dependency of the ADPs of the Zn and Sb atoms obtained from refinements of an independent atom model against high resolution x-ray data. In a perfect crystal, harmonic ADPs represent the anisotropic temperature factors and describe the mean-square vibrational amplitude of an atom with respect to its equilibrium position in the crystal. Figures 8(a) and 8(b) compare the diagonal elements of the U_{ij} tensor of the experimental ADPs and averaged U_{iso} values with ones derived from DFT calculations [Eqs. (5)–(8)]. The ratio of the calculated diagonal elements is qualitatively in agreement with the experiment (i.e., for the zinc atoms, $U_{11} > U_{22} \approx U_{33}$; for antimony atoms, $U_{33} \approx U_{22} > U_{11}$). The trend in

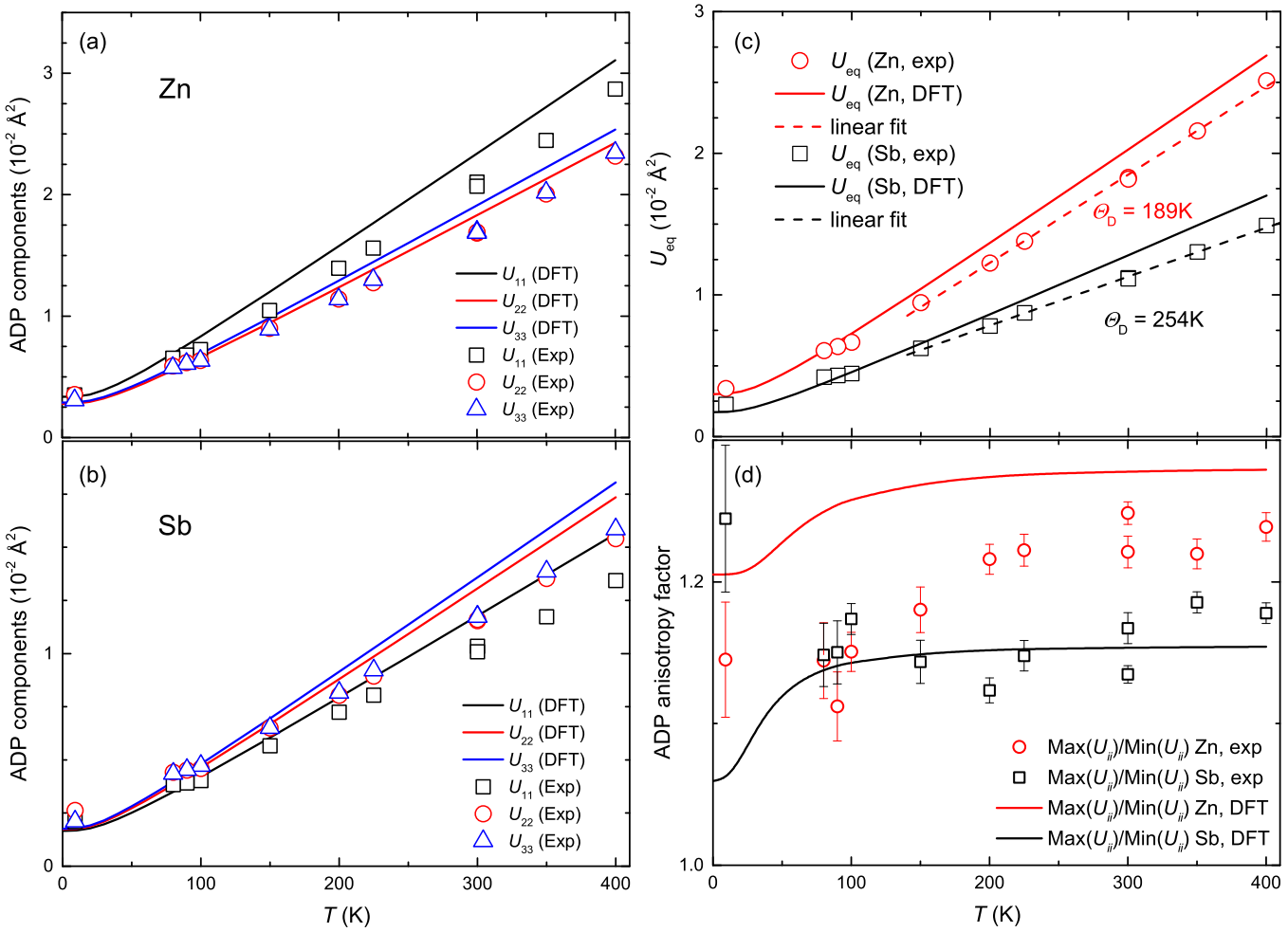

FIG. 8. (Color online) (a), (b) Theoretical harmonic ADPs obtained from DFT (solid lines) in comparison with experimental values; (c) comparison of U_{eq} values, which are calculated as the mean of the diagonal elements of the harmonic ADP tensor; and (d) comparison of the ADP anisotropy factor, which is defined as the ratio between maximum U_{ii} and minimum U_{ii} values. A ratio of 1 would correspond to an isotropic displacement.

temperature dependency of the absolute values of the U_{ij} tensor is also reproduced by the theoretical results. However, the calculated displacement parameters are slightly larger than the experimental ones at higher temperatures. ADP analysis reveals that the U_{ii} values of the Zn atom are, in general, larger than the corresponding ones of the antimony atoms at the same temperature, and they show a larger increase in magnitude with increasing temperature relative to the Sb atoms. This trend is consistent between the theoretical and experimental results and is therefore not significantly biased by a potential disorder of the Zn atoms, which would affect the experimental data only (which actually displays smaller U_{ii} values compared to the calculated ones by DFT). A severe deficiency of Zn atoms as another potential origin of the large U_{ii} values of Zn can be also ruled out since refinements against the high resolution diffraction data do not reveal any statistically significant deviation of the Zn atom site from full occupancy. Analysis of the ADPs obtained by experiment and the DFT calculation, however, cannot be used to furnish or preclude the presence of a deficient site occupancy of Zn due to defects. Indeed, reduction of the fractional site occupancy of Zn by 0.5% (which corresponds to an unrealistically high defect concentration of $1.03 \times 10^{20}\,\mathrm{cm}^{-3}$) causes a reduction of the corresponding U_{iso}(Zn) values by merely 0.7%, a value which is below statistical significance in the refinements of our x-ray data. Accordingly, the hypothesis that that electrical properties of ZnSb are largely influenced by the presence of Zn defects [6,54] can neither be confirmed nor ruled out on the basis of the x-ray data alone. Also, the presence of a severe substitutional Zn/Sb disorder is not indicated by our refinements. The latter case would be clearly indicated by an erroneous decrease of the U_{ii}(Zn) in the refinements and the presence of large residual densities in the core region of the zinc atoms [55]. Hence, the temperature dependent trend in the U_{ii} values is mainly attributed to the fact that the Zn atoms display a significantly smaller mass than the antimony atoms (most important isotopes: ^{64}Zn and ^{121}Sb). As a consequence, the theoretical U_{eq} value of the zinc atom, which is due to zero point motion, is already significantly larger (about 0.001 Å^2) than the corresponding U_{iso}(Sb) value at 0 K. This difference becomes even more pronounced at elevated temperature and reaches 0.01 Å^2 at 400 K.

It is common practice for the analysis of thermoelectric materials to use the slope of the individual $U_{\mathrm{eq}}(T)$ sequences [cf. Fig. 8(c)] to derive Debye and Einstein temperatures [56,57]. For the Debye case and $T > \Theta_D$, the temperature dependence of $U_{\mathrm{eq}}(T)$ corresponds to

$$U_{\mathrm{eq}}(T) = \frac{3h^2T}{4\pi^2 m_{\mathrm{at}} k_{\mathrm{B}} \Theta_{\mathrm{D}}^2}\,, \tag{12}$$

where m_{at} is the mass of the respective atoms in ZnSb. The derived Debye temperatures $\Theta_{\mathrm{D,exp,ADP}}$ using experimental $U_{\mathrm{eq}}(T)$ values above 150 K for ZnSb are 189 K and 254 K for Zn and Sb atoms, respectively. In the case of the DFT derived $U_{\mathrm{eq}}(T)$ values, the corresponding $\Theta_{\mathrm{D,theo,ADP}}$ values are 183 K and 230 K for Zn and Sb atoms, respectively. We note that the results for the Sb atoms compare reasonably well with the overall Debye temperature $\Theta_{\mathrm{D}}(0)$ from specific heat analysis (248 K from experiment and 210 K from DFT), while for Zn atoms the values are significantly lower. However, the difference between theory and experiment is more pronounced for Sb atoms.

In addition, the U_{ii} values of Zn atoms also increase in anisotropy, which is shown by the ratio of minimum and maximum U_{ii} values [cf. Fig. 8(d)]. The anisotropy for the DFT result is even higher but less temperature dependent above 80 K. For Sb atoms, the anisotropy is rather constant and agrees well with the DFT prediction.

When analyzing the residual density distributions of the harmonic refinements, we realized significant residual density features of positive and negative sign in alternating order at the Zn positions, which is a typical indicator for anharmonic motion [58]. This is shown in Fig. 9 (left panel). Third order (and corresponding higher order) ADPs, commonly known as the Gram-Charlier expansion, are used to describe this anharmonic motion. In the case of ZnSb, refinements of Gram-Charlier expansion of orders higher than three did not improve the flatness of the residual density maps significantly and were not pursued. Accordingly, only the third order anharmonic parameters were refined to model the ADPs of the zinc and antimony atoms. Since both Zn and Sb occupy general crystallographic positions, 10 third order anharmonic parameters per atom need to be considered. Their refinements helped to improve the data fit dramatically, as evidenced by the further decrease of the R value from 2.08 to 1.58% for the data collected at 400 K. As demonstrated in Fig. 9, the resulting residual electron density maps became essentially flat as a consequence of these anharmonic refinements. Analyses of the resulting probability density distributions do not reveal any pronounced negative regions, which is a prerequisite of a physically valid model [59].

Interestingly, only the Zn atoms are characterized by a significant anharmonicity of its vibrational amplitudes. The temperature dependency of the third order Gram-Charlier expansion coefficients for Zn are shown in Fig. 10(a). Although the Gram-Charlier expansion is a purely mathematical model without any expected temperature behavior, its parameters scale as T^2. This kind of temperature dependence can be expected, for example, for the potential parameters of a one particle anharmonic oscillator [60]. For Sb, all anharmonic parameters vanish within their standard uncertainty (see Supplemental Material [20]). The nuclear probability density of a Zn_2Sb_2 unit at 400 K is depicted in Fig. 10(b). We note that the refinement of anharmonic ADP has almost no influence on the values of the harmonic ADPs, in agreement with recent findings from theoretical models [61], and has only little influence on the interatomic distances [taken into account for in Fig. 2(c)]. Most notably, the Zn–Zn distance increases by 0.5% and the $r2$ distance by 0.3% compared to the purely harmonic model at a temperature of 400 K.

In conclusion, the refinement of anharmonic ADPs clearly validates the presence of anharmonicity in ZnSb. Moreover, the anharmonic behavior affects only the Zn atoms. Anharmonicity was already indicated from the analysis of the heat capacity and accounted for by introducing a A_1^{anh} parameter.

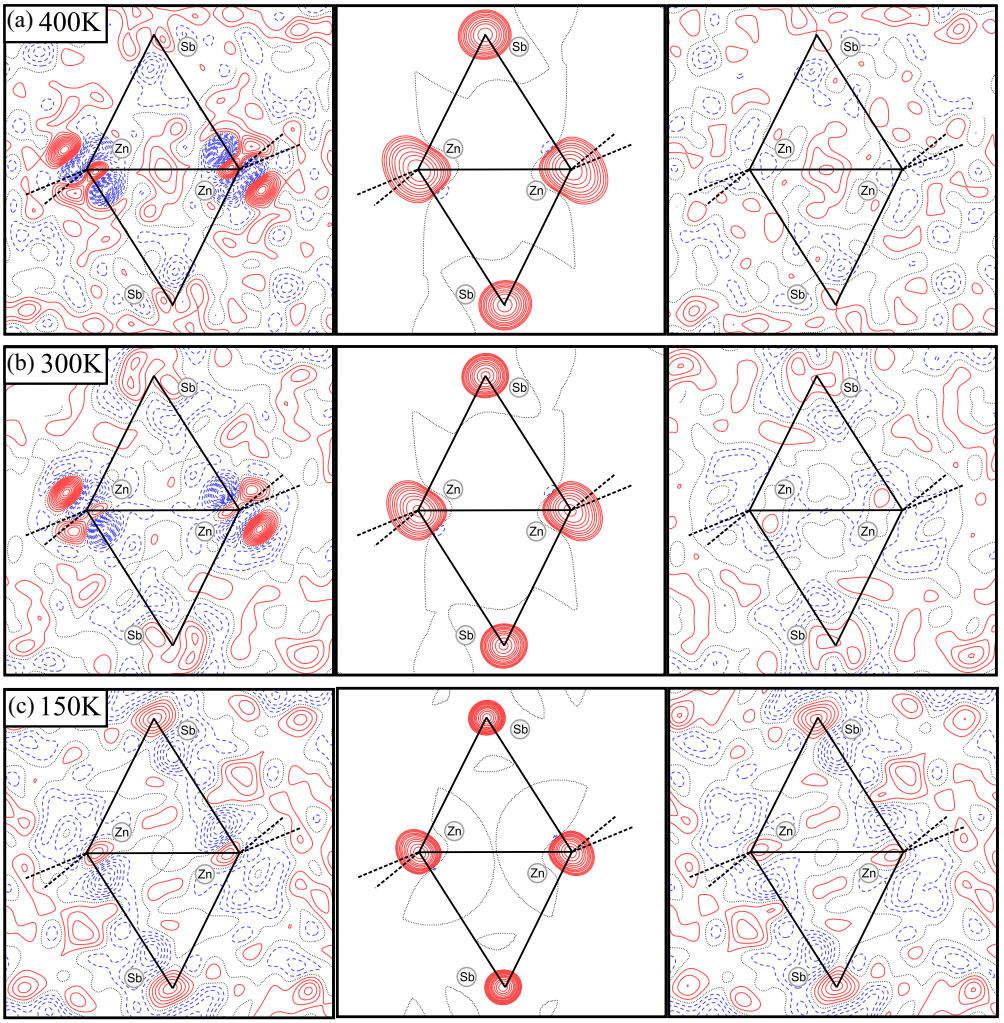

FIG. 9. (Color online) Difference electron density before (left) and after (right) anharmonic refinement for temperatures of 400 K, 300 K, and 150 K. The positive (red) and negative (blue) contour values are shown in $0.2e/\text{Å}^3$ steps. The probability density distribution (middle) is given with contour values $(2,4,8 \times 10^n\ \text{Å}^{-3}$, $n = -2,-1,0,1,2,3)$.

D. Origin of low thermal conductivity

The lattice thermal conductivity of ZnSb is remarkably low [6,62] and is characterized for temperatures above 200 K by values lower than 2 W/mK. This behavior of ZnSb compares well to bulk PbTe, which is one of the most established and approved thermoelectric materials. At first sight, rocksalt structured PbTe, which is exclusively constituted of heavy atoms, and ZnSb do not have much in common neither with regard to chemical composition nor with respect to structural chemistry. However, we argue that the physical mechanism, which is responsible for the low lattice thermal conductivity of both materials, is strikingly similar.

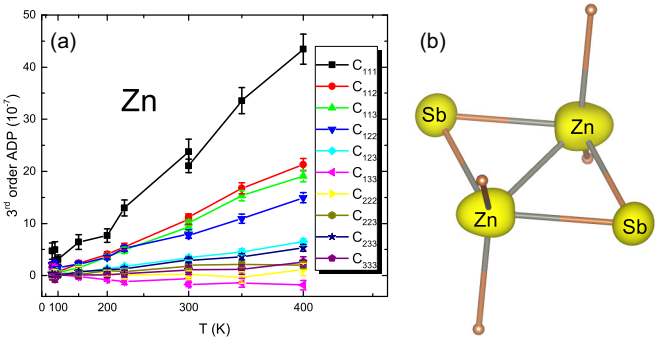

FIG. 10. (Color online) Third order Gram-Charlier ADP expansion coefficients for Zn (a) vs T (T axis scaled as T^2). Estimated standard uncertainties of the refined parameters are shown as error bars and (b) isosurface (surface value 0.1 Å^{-3}) representation of the nuclear probability density of the Zn_2Sb_2 entity at 400 K.

Recent inelastic neutron scattering experiments on PbTe revealed a peculiar dynamic behavior: Through anharmonic coupling the ferroelectric transverse optic (TO) mode interacts with the heat carrying longitudinal acoustic phonons over a wide range of frequencies, thus resembling a rattling mode [63]. Other studies showed disorder for the Pb atoms, which displace increasingly with temperature from their ideal position in the rocksalt structure [64,65]. The dynamical peculiarity and structural disorder are certainly correlated and have been interpreted by considering PbTe as an incipient ferroelectric material [63]. The incipient ferroelectric state in turn is a consequence of Pb $6p$-Te $5p$ bonding.

We propose that the role of the ferroelectric TO mode in PbTe is adopted by weakly dispersed low-energy optic modes in ZnSb. Their presence is a natural consequence of localized multicenter bonding established within the rhomboid Zn_2Sb_2 rings. The peculiar feature of the PDOS of ZnSb is the accumulation of 12 optic modes in a narrow window between 36 and 61 cm^{-1}. This assembly of 12 soft modes possesses a great flexibility, which allows for effective interaction with heat carrying acoustic phonons throughout large parts of the Brillouin zone (cf. Fig. 6). Further, there is an increasing anharmonicity of the mean-square vibrational amplitudes of the zinc atoms with rising temperature in the diffraction experiments. Also, this phenomenon is likely to be inherent to the electron-poor bonding properties of ZnSb and provides additional possibilities for phonon-phonon interactions. First, additional (symmetry forbidden) interaction of optic and acoustic modes will be allowed by anharmonic coupling. Second, phonon-phonon scattering (umklapp processes) are promoted at higher temperatures (typically above Θ_D).

In conclusion, there appears to be a great analogy in the mechanism causing low lattice thermal conductivity for PbTe and ZnSb, despite their distinctly different chemical composition and structures. Moreover, we believe that the peculiar phononic structure of ZnSb (displaying a multitude of localized low-energy modes, which can act as rattling modes toward heat carrying acoustic phonons) represents the sought-after underlying characteristic that accounts generally for an inherent low lattice thermal conductivity for zinc antimony compound and their derivatives. The presence of localized low-energy optic modes is seen as a consequence of multicenter bonded structural entities, which are common to all these compounds.

IV. CONCLUSION

ZnSb possesses an inherently low lattice thermal conductivity, which is related in nature and magnitude to the one observed in the state-of-the-art thermoelectric material PbTe. From a combination of high resolution XRD studies, Raman spectroscopy, heat capacity measurements, and first principles calculations of the electronic and phononic structure, we identify peculiar electronic and vibrational properties as control parameters of the thermoelectric properties of ZnSb. These properties manifest themselves in a multitude of localized low-energy optic modes (which couple with the acoustic, heat carrying phonons) and an anharmonic vibrational behavior of the Zn atoms. Both facets are regarded as a natural consequence of the electron-poor character of multicenter bonded structural Zn_2Sb_2 entities. Such entities are a common feature of thermoelectric electron poor semiconductors. We therefore argue that the vibrational behavior of ZnSb directly correlates with its bonding properties and that the established mechanisms for low thermal conductivity can be extended to other thermoelectric electron poor semiconductors like Zn_4Sb_3, CdSb, Cd_4Sb_3, $Cd_{13-x}In_yZn_{10}$, and $Zn_5Sb_4In_{2-\delta}$.

ACKNOWLEDGMENTS

This paper was supported by the US National Science Foundation (NSF-DMR-1007557), the Swedish Research Council (2010-4827 and 2013-4690), and the Deutsche Forschungsgemeinschaft (DFG; SCHE 487/12-1).

[1] D. N. Nasledov and V. Y. Shevchenko, Phys. Status Solidi A **15**, 9 (1973).
[2] E. K. Arushanov, Prog. Cryst. Growth Charact. **13**, 1 (1986).
[3] B. B. Iversen, J. Mater. Chem. **20**, 10778 (2010).
[4] E. S. Toberer, P. Rauwel, S. Gariel, J. Taftø, and G. Jeffrey Snyder, J. Mater. Chem. **20**, 9877 (2010).
[5] T. Caillat, J.-P. Fleurial, and A. Borshchevsky, J. Phys. Chem. Solids **58**, 1119 (1997).
[6] D. Eklöf, A. Fischer, Y. Wu, E.-W. Scheidt, W. Scherer, and U. Häussermann, J. Mater. Chem. A **1**, 1407 (2012).
[7] K. Valset, P. H. M. Böttger, J. Taftø, and T. G. Finstad, J. Appl. Phys. **111**, 023703 (2012).
[8] D.-B. Xiong, N. L. Okamoto, and H. Inui, Scr. Mater. **69**, 397 (2013).
[9] G. J. Snyder, M. Christensen, E. Nishibori, T. Caillat, and B. B. Iversen, Nat. Mater. **3**, 458 (2004).
[10] A. Tengå, S. Lidin, J.-P. Belieres, N. Newman, Y. Wu, and U. Häussermann, J. Am. Chem. Soc. **130**, 15564 (2008).
[11] W. Schweika, R. P. Hermann, M. Prager, J. Perßon, and V. Keppens, Phys. Rev. Lett. **99**, 125501 (2007).
[12] E. Chalfin, H. Lu, and R. Dieckmann, Solid State Ionics **178**, 447 (2007).
[13] J. Lin, X. Li, G. Qiao, Z. Wang, J. Carrete, Y. Ren, L. Ma, Y. Fei, B. Yang, L. Lei, and J. Li, J. Am. Chem. Soc. **136**, 1497 (2014).
[14] Y. Wu, S. Lidin, T. L. Groy, N. Newman, and U. Häussermann, Inorg. Chem. **48**, 5996 (2009).
[15] Y. Wu, A. Tengå, S. Lidin, and U. Häussermann, J. Solid State Chem. **183**, 1574 (2010).
[16] U. Häussermann and A. S. Mikhaylushkin, Dalton Trans. **39**, 1036 (2010).
[17] P. Jund, R. Viennois, X. Tao, K. Niedziolka, and J.-C. Tédenac, Phys. Rev. B **85**, 224105 (2012).
[18] L. Bjerg, B. B. Iversen, and G. K. H. Madsen, Phys. Rev. B **89**, 024304 (2014).
[19] V. Petříček, M. Dušek, and L. Palatinus, Z. Kristallogr. **229**, 345 (2014).
[20] See Supplemental Material at http://link.aps.org/supplemental/10.1103/PhysRevB.91.224309 for tables on the temperature dependent PXRD/SXRD measurements and refinements.
[21] *SAINT v7.68A* (Bruker AXS Inc., Madison, Wisconsin, USA, 2008).
[22] *SADABS v2008/2* (G. M. Sheldrick, Göttingen, 2008).
[23] A. M. M. Schreurs, X. Xian, and L. M. J. Kroon-Batenburg, J. Appl. Crystallogr. **43**, 70 (2010).
[24] A. L. Spek, J. Appl. Crystallogr. **36**, 7 (2003).
[25] X. Gonze, B. Amadon, P.-M. Anglade, J.-M. Beuken, F. Bottin, P. Boulanger, F. Bruneval, D. Caliste, R. Caracas, M. Côté, T. Deutsch, L. Genovese, P. Ghosez, M. Giantomassi, S. Goedecker, D. R. Hamann, P. Hermet, F. Jollet, G. Jomard, S. Leroux *et al.*, Comput. Phys. Commun. **180**, 2582 (2009).

[26] X. Gonze, Z. Kristallogr. **220**, 558 (2005).
[27] X. Gonze, J.-M. Beuken, R. Caracas, F. Detraux, M. Fuchs, G.-M. Rignanese, L. Sindic, M. Verstraete, G. Zerah, F. Jollet, M. Torrent, A. Roy, M. Mikami, P. Ghosez, J.-Y. Raty, and D. C. Allan, Comput. Mater. Sci. **25**, 478 (2002).
[28] Y. Wang and J. P. Perdew, Phys. Rev. B **44**, 13298 (1991).
[29] J. P. Perdew, K. Burke, and M. Ernzerhof, Phys. Rev. Lett. **77**, 3865 (1996).
[30] M. Fuchs and M. Scheffler, Comput. Phys. Commun. **119**, 67 (1999).
[31] H. J. Monkhorst and J. D. Pack, Phys. Rev. B **13**, 5188 (1976).
[32] X. Ke and I. Tanaka, Phys. Rev. B **71**, 024117 (2005).
[33] N. Ohba, K. Miwa, T. Noritake, and A. Fukumoto, Phys. Rev. B **70**, 035102 (2004).
[34] K. E. Almin, N. Hofman-Bang, and P. Gjertsen, Acta Chem. Scand. **2**, 400 (1948).
[35] D. Benson, O. F. Sankey, and U. Häussermann, Phys. Rev. B **84**, 125211 (2011).
[36] A. S. Mikhaylushkin, J. Nylén, and U. Häussermann, Chem. Eur. J. **11**, 4912 (2005).
[37] ELK-Code Version 2.2.10 (2014).
[38] M. Kohout, *DGrid v4.6e* (Radebeul, Germany, 2011).
[39] W. Scherer and G. S. McGrady, Angew. Chem. Int. Ed. **43**, 1782 (2004).
[40] R. F. W. Bader, T. T. Nguyen-Dang, and Y. Tal, Rep. Prog. Phys. **44**, 893 (1981).
[41] J.-B. Li, M.-C. Record, and J.-C. Tedenac, J. Alloys Compd. **438**, 171 (2007).
[42] Y. Mozharivskyj, A. O. Pecharsky, S. Bud'ko, and G. J. Miller, Chem. Mater. **16**, 1580 (2004).
[43] K. M. Mamedova, A. Yu. Dzhangirov, O. I. Dzhafarov, and V. N. Kostryukov, Russ. J. Phys. Chem. **49**, 1635 (1975).
[44] G. N. Danilenko, V. Ya. Shevchenko, S. F. Marenkin, and M. Kh. Karapet'yants, Inorg. Mater. **14**, 486 (1978).
[45] K. K. Kelley and E. G. King, *Contributions to the Data on Theoretical Metallurgy: Part 14. Entropies of the Elements and Inorganic Compounds* (U.S. Government Printing Office, Washington, DC, 1961).
[46] R. Pässler, J. Phys. Chem. Solids **72**, 1296 (2011).
[47] R. Pässler, AIP Adv. **3**, 082108 (2013).
[48] V. N. Balazyuk, A. I. Eremenko, and N. D. Raransky, Funct. Mater. **15**, 343 (2008).
[49] O. L. Anderson, J. Phys. Chem. Solids **12**, 41 (1959).
[50] D. T. Morelli and G. A. Slack, in *High Thermal Conductivity Materials*, edited byS. L. Shindé and J. S. Goela (Springer, New York, 2006), pp. 37–68.
[51] D. V. Smirnov, D. V. Mashovets, S. Pasquier, J. Leotin, P. Puech, G. Landa, and Y. V. Roznovan, Semicond. Sci. Technol. **9**, 333 (1994).
[52] D. Houde, J. Lefaivre, S. Jandl, and E. Arushanov, Solid State Commun. **41**, 325 (1982).
[53] D. M. Trichês, S. M. Souza, J. C. de Lima, T. A. Grandi, C. E. M. Campos, A. Polian, J. P. Itié, F. Baudelet, and J. C. Chervin, J. Appl. Phys. **106**, 013509 (2009).
[54] L. Bjerg, G. K. H. Madsen, and B. B. Iversen, Chem. Mater. **24**, 2111 (2012).
[55] A. Haaland, K. Rypdal, H. P. Verne, W. Scherer, and W. R. Thiel, Angew. Chem. Int. Ed. Engl. **33**, 2443 (1995).
[56] B. C. Sales, B. C. Chakoumakos, D. Mandrus, and J. W. Sharp, J. Solid State Chem. **146**, 528 (1999).
[57] B. C. Sales, D. G. Mandrus, and B. C. Chakoumakos, Semicond. Semimet. **70**, 1 (2001).
[58] K. Meindl, R. Herbst-Irmer, and J. Henn, Acta Crystallogr. Sect. A **66**, 362 (2010).
[59] R. Bachmann and H. Schulz, Acta Crystallogr. A **40**, 668 (1984).
[60] P. Coppens, *X-Ray Charge Densities and Chemical Bonding* (International Union of Crystallography/Oxford University Press, Oxford, 1997).
[61] D. J. Safarik, A. Llobet, and J. C. Lashley, Phys. Rev. B **85**, 174105 (2012).
[62] P. H. M. Böttger, G. S. Pomrehn, G. J. Snyder, and T. G. Finstad, Phys. Status Solidi A **208**, 2753 (2011).
[63] O. Delaire, J. Ma, K. Marty, A. F. May, M. A. McGuire, M.-H. Du, D. J. Singh, A. Podlesnyak, G. Ehlers, M. D. Lumsden, and B. C. Sales, Nat. Mater. **10**, 614 (2011).
[64] E. S. Božin, C. D. Malliakas, P. Souvatzis, T. Proffen, N. A. Spaldin, M. G. Kanatzidis, and S. J. L. Billinge, Science **330**, 1660 (2010).
[65] S. Kastbjerg, N. Bindzus, M. Søndergaard, S. Johnsen, N. Lock, M. Christensen, M. Takata, M. A. Spackman, and B. Brummerstedt Iversen, Adv. Funct. Mater. **23**, 5477 (2013).